

# Anatomically-Informed Deep Learning on Contrast-Enhanced Cardiac MRI for Scar Segmentation and Clinical Feature Extraction

Haley G. Abramson<sup>1,†</sup>, Dan M. Popescu<sup>2,†</sup>, Rebecca Yu<sup>3</sup>, Changxin Lai<sup>1</sup>, Julie K. Shade<sup>1</sup>, Katherine C. Wu<sup>4</sup>, Mauro Maggioni<sup>2</sup>, and Natalia A. Trayanova<sup>1</sup>

<sup>†</sup>These authors contributed equally to this work

<sup>1</sup>Department of Biomedical Engineering, Johns Hopkins University School of Medicine, Baltimore, MD, 21205, USA.

<sup>2</sup>Department of Applied Mathematics and Statistics, Johns Hopkins University, Baltimore, MD, 21218, USA.

<sup>3</sup>Department of Biomedical Engineering, Johns Hopkins University, Baltimore, MD, 21218, USA.

<sup>4</sup>Division of Cardiology, Department of Medicine, Johns Hopkins Hospital, Baltimore, MD, 21205, USA.

## ABSTRACT

Many cardiac diseases are associated with structural remodeling of the myocardium. Cardiac magnetic resonance (CMR) imaging with contrast enhancement, such as late gadolinium enhancement (LGE), has unparalleled capability to visualize fibrotic tissue remodeling, allowing for direct characterization of the pathophysiological abnormalities leading to arrhythmias and sudden cardiac death (SCD). Automating segmentation of the ventricles with fibrosis distribution could dramatically enhance the utility of LGE-CMR in heart disease clinical research and in the management of patients with risk of arrhythmias and SCD. Here we describe an anatomically-informed deep learning (DL) approach to myocardium and scar segmentation and clinical feature extraction from LGE-CMR images. The technology enables clinical use by ensuring anatomical accuracy and complete automation. Algorithm performance is strong for both myocardium segmentation (98% accuracy and 0.79 Dice score in a hold-out test set) and evaluation measures shown to correlate with heart disease, such as scar amount (6.3% relative error). Our approach for clinical feature extraction, which satisfies highly complex geometric constraints without stunting the learning process, has the potential of a broad applicability in computer vision beyond cardiology, and even outside of medicine.

## Introduction

Many cardiac diseases are associated with structural remodeling of the myocardium. In both ischemic and non-ischemic cardiomyopathies, the proliferation of myocardial fibrosis (scarring) has been found to significantly elevate the risk for lethal heart rhythm disorders and sudden cardiac death (SCD)<sup>1–5</sup>. Identifying and characterizing fibrotic remodeling in the heart is of great clinical decision-making value, as it allows to assess arrhythmia propensity and stratify patients for SCD risk<sup>1,2,6</sup>.

Cardiac magnetic resonance (CMR) imaging with contrast enhancement, such as late gadolinium enhancement (LGE), has unparalleled capability to visualize fibrotic tissue remodeling<sup>7</sup>, allowing for direct characterization of the pathophysiological abnormalities leading to arrhythmias and SCD. A large body of research<sup>4,8–11</sup> has demonstrated the utility of fibrosis characterization via LGE-CMR in advancing our understanding of the mechanisms underlying arrhythmogenesis, and in the diagnosis and treatment of cardiac arrhythmias.

Currently, delineating myocardium and fibrotic tissue in LGE-CMR images demands time-intensive manual labor and has high variability across experts<sup>12,13</sup>. This variance stems from inconsistent image quality across centers, frequent imaging artifacts, and ambiguous myocardial boundaries under enhancement. Both blood pool and scar have high intensities with LGE, posing a challenge for humans and computer programs alike to distinguish the endocardial border<sup>14</sup> and hindering the use of traditional thresholding methods<sup>15,16</sup>. The substantial inter-observer variability is further exacerbated by the fact that low-intensity, viable myocardium is co-localized within the same anatomical structure with high-intensity fibrotic tissue. Image segmentation methods such as region growing require individually selected parameters for each scan due to contrast inconsistencies across MR scanners and imaging centers, in addition to demanding significant computational costs<sup>17,18</sup>. Automating segmentation of the ventricles with fibrosis distribution could dramatically enhance the utility of LGE-CMR in heart disease clinical research and in the management of patients with risk of arrhythmias and SCD.

Deep learning (DL) applied to cardiac image segmentation offers the promise of full automation and consistency of output<sup>19</sup>. However, most of the available algorithms require intensive manual interventions, *e.g.*, specifying anatomical landmarks<sup>20</sup>

or labeling boundary slices of the stack at the apex and base of the heart<sup>21</sup>. The few DL algorithms developed for LGE-CMR myocardium segmentation<sup>14,22–24</sup> and the even fewer for LGE-CMR scar segmentation<sup>25,26</sup> all suffer from significant limitations. Specifically, these approaches are not robust to varying image acquisition quality (*i.e.*, different scanners and protocols at different centers) or to the varying fibrosis patterns resulting from different heart pathologies, leading to bespoke algorithms which fail to generalize across populations<sup>25</sup>. Additionally, poor quality and quantity of LGE-CMR datasets can impair data-intensive DL algorithms, further diminishing segmentation accuracy and scar tissue recognition. Furthermore, because success has been measured by broad study-wide averages that often elicit poor-performing outliers<sup>27</sup>, anatomical fidelity of computer-generated cardiac segmentations is often compromised<sup>25</sup>, resulting in inability to extract features of significance to clinical decision-making. Therefore, a data-efficient, automated algorithm for anatomically-accurate LGE-CMR segmentation of myocardium and scar remains an unmet clinical need.

Here we describe an anatomically-informed deep-learning (DL) approach to myocardium and scar segmentation and clinical feature extraction from LGE-CMR images. We term our technology Anatomical Convolutional Segmentation Network, ACSNet. The technology enables clinical use by ensuring anatomical accuracy and complete automation. It is robust to inputs from different CMR modalities and imaging centers, and scar distributions arising from different heart pathologies. Unlike existing LGE-CMR segmentation technologies, ours accurately quantifies scar and calculates ventricular volume, outperforming inter-expert results without compromising the anatomical integrity of the segmentation. By eliminating manual interventions, this approach holds the potential to democratize cardiac diagnostic radiology by providing reliable prognostic results and bridging inequity in healthcare delivery. Furthermore, ACSNet's approach for clinical feature extraction, which satisfies highly complex geometric constraints without stunting the learning process, has the potential of a broad applicability in computer vision beyond cardiology, and even outside of medicine.

## Anatomically-Informed Deep Learning Model

ACSNet uses three inter-connected DL sub-networks that progressively refine the left ventricle (LV) myocardium and scar segmentation from the LGE-CMR images. The input to the first DL sub-network is the result of an innovative data augmentation process, which overcomes the scarcity of public LGE-CMR scans by transforming more readily available CMR cine scans into “LGE-like” images. To accomplish this, we developed a low-cost cine-to-LGE conversion algorithm that adds pseudo-enhancement to non-enhanced cine, thus mitigating the imbalance between LGE and cine data availability. The process tripled the available dataset to 400 patient scans, amounting to 2,484 images<sup>28–30</sup>, acquired by a wide variety of imaging protocols in heterogeneous patient populations.

The first network in ACSNet handles the overwhelmingly high ratio of background pixels to myocardium by identifying the LV and cropping each image tightly around it (fig. 1A). The second network then uses the tightly cropped image to differentiate blood pool, viable myocardium, and hyper-enhanced scar, returning segmentations for both tissue types (fig. 1B). The third network is a convolutional autoencoder which refines the shape of myocardium and scar in each slice and in the total volume (fig. 1C).

Correct training segmentations are encoded into the autoencoder latent space, which we then model as a mixture of Gaussian distributions. We populate the latent space via an anatomically-informed rejection sampling scheme within the Gaussian mixture model (GMM) (fig. 1D). Upon predicting a new segmentation, we encode the input image and perturb the point in the encoding space in the direction of the closest point in the population sampled from the constrained GMM until anatomical constraints are fulfilled by the point's decoded image representation, the latter being the final post-processed output. As a result, predicted segmentations by ACSNet pass complex whole-ventricle anatomical requirements such as circularity and minimum thickness (see Methods), which not only ensure anatomical accuracy, but also allow for proper handling of ambiguous regions (*e.g.*, apex and base), where observer ground truth variability is high due primarily to imaging artifacts.

## Application-Driven Evaluation of the Technology

ACSNet's performance was demonstrated by testing only on out-of-sample LGE-CMR scans (269 images, 25% of LGE cohort) that have the capability of visualizing scar, while both cine-converted “LGE-like” and LGE-CMR images were used during training (2,484 images). LV network segmentation, which includes blood pool, viable, and non-viable tissue, received Dice scores of 0.96 and 0.92 in training (on both LGE-CMR and cine) and testing (on LGE-CMR), respectively. Before anatomical post-processing by the third sub-network, the LV myocardium network trained to a Dice score of 0.91 and tested on LGE-CMR images with a Dice score of 0.79 for myocardium segmentation. Results from the autoencoder and morphological post-processing steps maintained a Dice score of  $0.79 \pm 0.02$ , with 98% accuracy and 69% precision (fig. 2). The Hausdorff distance (HD) measured from ACSNet predictions ( $6.76 \pm 0.46\text{mm}$ ) was lower than that of previously recorded LGE-CMR segmentation methods (table 1), indicating increased similarity between predicted and ground truth segmentations. Thus, ACSNet improved upon both the inter-observer Dice score of 0.76 as well as the inter-observer HD ( $10.6 \pm 4.65$  endocardial

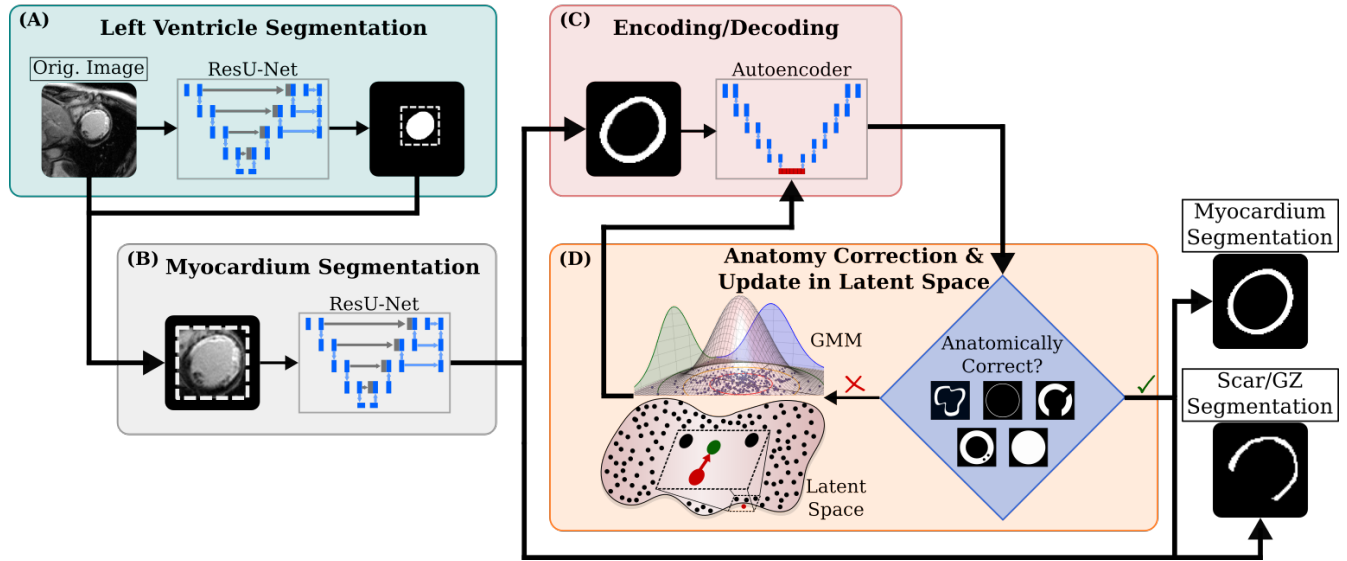


**Figure 1. ACSNet architecture.** (A) The first residual U-Net (ResU-Net) serves to identify and crop around the left ventricle. (B) A sequential network then differentiates viable and hyper-enhanced myocardium, returning segmentations for all myocardial tissue and for scar and gray zone (GZ). (C) Myocardial segmentations are encoded/decoded via a convolutional autoencoder. (D) A latent space is formed using encoded segmentations from the training set. The space is modeled as a Gaussian Mixture Model (GMM) and conditional re-sampling is performed to fill the space with anatomically correct samples (black dots). Predicted segmentations are encoded and the nearest neighbors algorithm is used to return a perturbed, anatomically correct version (green dot) of the original (red dot). GMM image adapted from source<sup>31</sup>.

HD and  $12.5 \pm 5.38$  epicardial HD) recorded in the Multi-Sequence Cardiac MRI Segmentation (MS-CMRSeg) Challenge<sup>12,13</sup>. While comparable Dice scores between ACSNet and existing DL applications indicate a level playing field (table 1), the power of ACSNet lies in its consistency of segmentation across all LV regions and its guarantee of anatomical accuracy, which has not been previously achieved for LGE-CMR. Our results demonstrate no statistically significant difference between features calculated using automatic vs. manual segmentations. LV volume calculations result in a relative mean squared error (MSE) of 4.0%. Scar quantification has a relative MSE of 6.3% (fig. 3).

## Discussion

In this study we present a clinical-application-driven approach for automatic segmentation, with high anatomical accuracy, of myocardium and fibrosis in LGE-CMR images and for extracting anatomical features that are essential for disease diagnosis and clinical decision-making. ACSNet is a cascade of three neural networks that progressively refine LV viable and non-viable tissue segmentations and constrain results within anatomical guidelines for both individual slices and LV volume. These constraints prevent poorly segmented outliers that can arise particularly at the apex and base. Additionally, the diverse training set used in ACSNet enhances the network's robustness, expanding its ability to be successfully used in unseen patient populations. Our technology can be seamlessly employed to extract salient anatomical features, potentially enhancing the diagnostic utility of LGE-CMR.

There are innovations at every step in our technology that help boost ACSNet's performance. In LGE-CMR image pre-processing, we automatically apply contrast and brightness adjustments to images if these are stored as tags on the particular image's header. Further, we augment our training dataset by generating "LGE-like" images from cine, improving performance on the LGE-CMR test set. The complex learning process is divided into three sub-networks, each having distinct tasks: the first reduces class imbalance between the region of interest and background, the second delineates endocardium and epicardium, and the third ensures anatomical correctness for both slices and volumes. The third neural sub-network expands on previous work<sup>32</sup> originally developed for cine segmentation by incorporating multiple highly complex 2-D and 3-D geometrical constraints, implementing a smaller non-variational network that does not require knowledge of slice location, and simplifying the structure and modeling of the latent space.

The current limitations in cine-based segmentation approaches, such as their requirements for additional types of ground-truth labels, poor performance in the more challenging apical and basal regions, and anatomically inaccurate results, prevent their adoption in LGE-CMR segmentation. For example, the method of Zheng *et al.*<sup>21</sup> requires a pre-processing step to discard

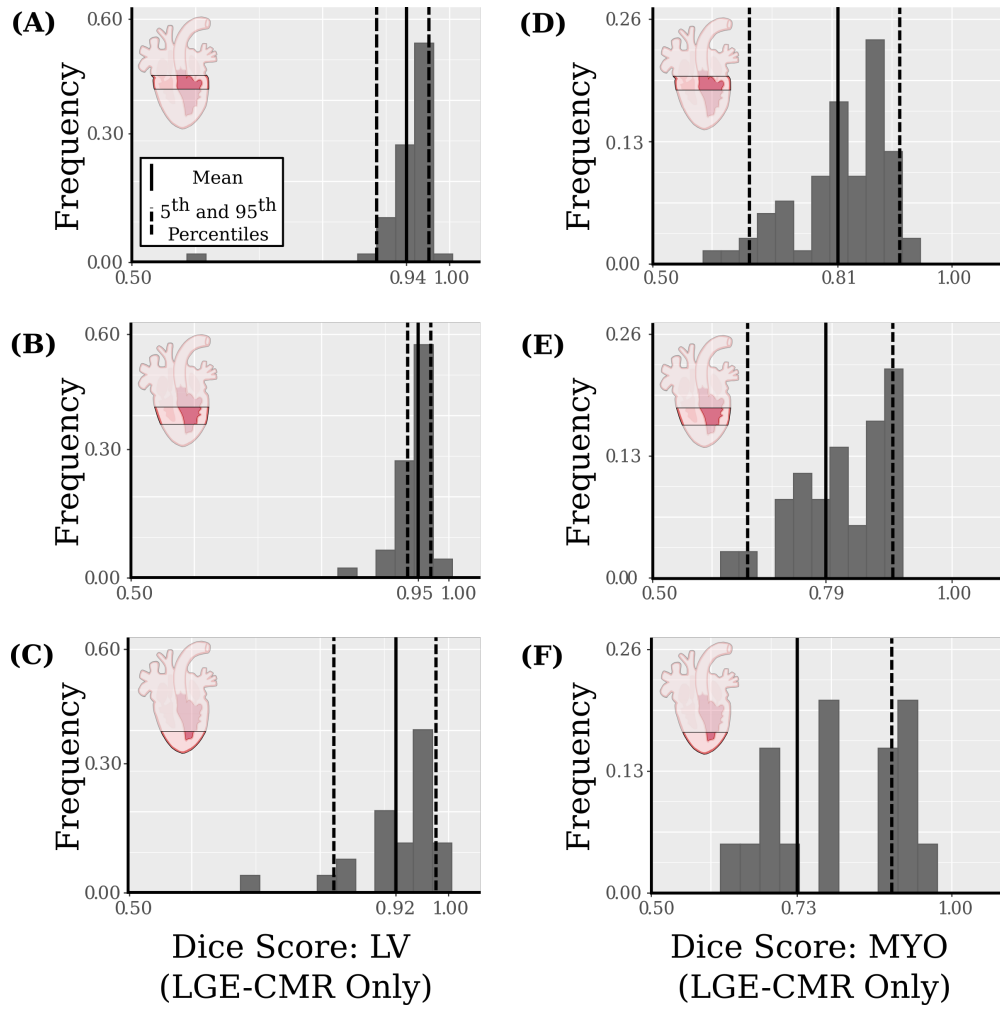


**Figure 2. Segmentation Results.** Histograms of Dice score values are shown per slice for the test set, separated by region of the heart as indicated. (A-C) Dice scores are shown for the left ventricle (LV) and (D-F) myocardium (MYO). The averages (solid vertical lines) for each region are 0.94 (A) and 0.81 (D) in the base, 0.95 (B) and 0.79 (E) in the middle, and 0.92 (C) and 0.73 (F) in the apex.

apical and basal slices and a manual curation of “difficult cases”. Similarly, Bello *et al.*<sup>20</sup> rely on ground-truth anatomical landmark localization. Without such additional annotations in the training data, there is no control on anatomically inconsistent outliers. Recent methods have proposed post-processing steps to improve the anatomical accuracy of myocardium segmentations from cine images<sup>32,33</sup>. Although these algorithms smooth out resulting segmentations, they use generic techniques unable to capture nuances of heart anatomy<sup>33</sup>; they require an already highly accurate segmentation as input to function well<sup>32</sup>; or they do not incorporate 3-D constraints<sup>32</sup>. Furthermore, effective LGE-CMR DL segmentation methods are very scarcely available for myocardium and virtually nonexistent for fibrosis. Approaches such as Campello *et al.*<sup>14</sup> — which uses a CycleGAN<sup>34</sup> to transform cine into “LGE-like” images — partially address the LGE-CMR data scarcity to obtain accurate myocardium segmentations, but, in the process, the approach loses the fibrosis features, the salient aspect of LGE-CMR. In our attempt to implement CycleGAN for the cine-to-LGE conversion, we obtained less than 1% Dice coefficient improvement in LV myocardium segmentation. Very recently, Zabihollahy *et al.*<sup>25</sup> have attempted myocardium and scar segmentation on 3-D LGE-CMR, but, despite the benefit of a 10-fold increase in the number of short-axis slices per patient, their results show several artifacts, such as disjoint pieces of myocardium. Moccia *et al.*<sup>26</sup> required manually segmented ground truth myocardium as an additional network input to predict scar segmentations and used only 30 patients, all from a single center, split across training and testing. ACSNet overcomes these limitations by providing an efficient DL segmentation algorithm requiring the standard-of-care widely used 2-D LGE-CMR scans to produce consistent, anatomically accurate results.

Despite the complexity of LGE-CMR images, we achieved a high Dice score when testing on them. We improved on

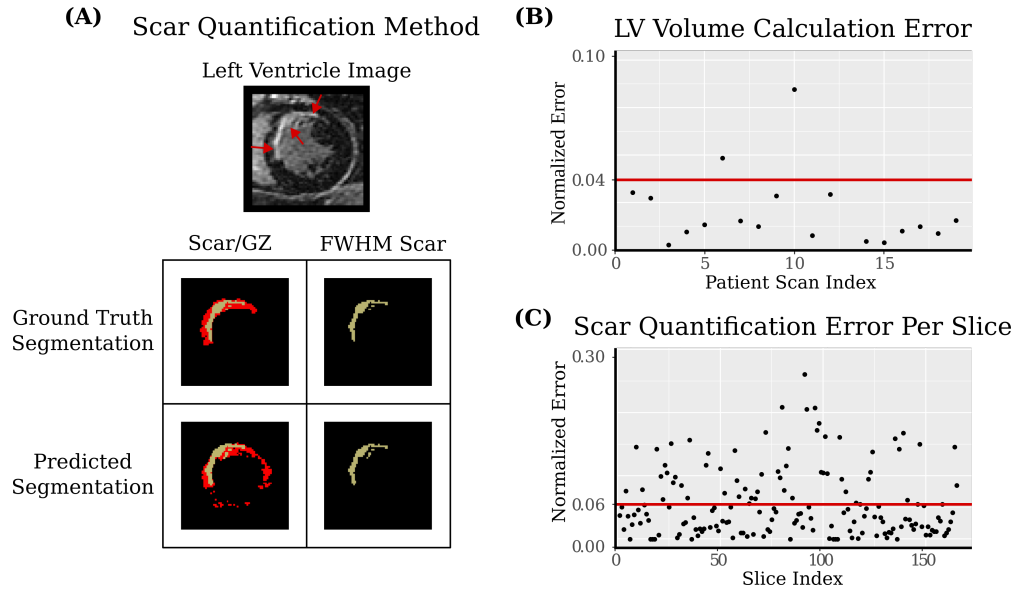


**Figure 3. Scar Quantification and Volume Calculation.** (A) Fibrotic segmentation predictions from the left ventricle (LV) network represent gray zone (GZ, red) and scar (gold), the latter of which is then quantified by thresholding at the full width-half maximum (FWHM) intensity value of the masked image and compared to ground truth. (B) LV volume was calculated using myocardium and blood pool from both predicted and manual segmentations. The normalized root MSE was 0.040 (red line). Each point represents the error in volume of a single segmented patient scan. (C) All scar quantification errors per slice are plotted. The normalized root MSE is 0.063 (red line). Error for both volume and scar is calculated as the error normalized by the  $\ell_2$  norm.

inter-observer scores<sup>12,13</sup> and quantified scar with low error (6.3%), while maintaining a high degree of anatomical accuracy. Generalization across patient cohorts, MR scanners (*e.g.*, Siemens<sup>®</sup> and General Electric<sup>®</sup>), and health centers is often a concern when developing DL algorithms. We mitigate this challenge by training with numerous datasets<sup>28–30</sup> acquired with different imaging protocols. An additional obstacle associated with image segmentation is training well when inter-observer variability is high, *i.e.*, when ground truth data is noisy. Rather than replicating the noisy ground truth, our network focuses on generating reliable segmentations, which we demonstrate through high performance on both Dice score (fig. 2) and clinical feature extraction (fig. 3). We avoid potential overfitting when building the network by not performing a broad hyperparameter sweep. Exploration of different hyperparameter implementations demonstrated similar Dice score results, thereby indicating the robustness of the core ACSNet model.

Incorporating complex constraints into a DL algorithm may be broadly applied to many computer vision problems. Convolutional neural networks face challenges in learning non-differentiable functions such as ACSNet’s anatomical checks; they face similar challenges in, for example, inverse problems or 3-D scene rendering. In applications beyond medicine such as programming an autonomous vehicle to identify pedestrians in a street scene or modeling planets as imperfect spheres, our method has potential to be utilized in any problem demanding specific guidelines from predicted outputs.

## Methods

ACSNet uses a 3-stage adaptive approach to segment viable myocardium, enhanced myocardium (gray zone and scar), and blood pool: (1) one network identifies the LV used to reduce extraneous information; (2) a refinement network differentiates between tissue types; and (3) a post-processing stage updates the predictions under anatomical constraints. Novel pre-processing steps increase model performance on LGE–CMR images, and additional post-processing volumetric guidelines ensure realistic whole-ventricle segmentations.

### Data Source and Preparation

We have developed an innovative data augmentation step to prepare images for the first sub-network. End diastole (ED) cine images with manual LV myocardial segmentations from the MICCAI ACDC<sup>28</sup> and Sunnybrook datasets<sup>29</sup> are used jointly with LGE–CMR images provided by the PROSE-ICD dataset (Prospective Observational Study of Implantable Cardioverter Defibrillators, NCT00733590), which include both ground truth myocardium and fibrosis segmentations, to train ACSNet.



Due to the large amounts of data required by deep learning algorithms, numerous medical image file types, and scattered sources of available data, we pre-process all images by storing them in a universally accessible format. ACSNet networks use 2-D inputs, though patient information is stored as a volume for ease in pre- and post-processing. Slices are ordered apex to base (in the increasing short axis direction) with slice location, image intensities, resolution, and patient orientation. Slices with no ground truth segmentation are excluded. Eliminating non-existent segmentations tailors the network towards learning how to identify myocardium as opposed to learning whether a segmentation exists. We then rely on comprehensive volumetric checks (described below) to trim extraneous slices below the apex and above the base.

Rotation and brightness pre-processing steps standardize the data. Each scan is rotated an increment of 90 degrees to approximate a reference orientation while avoiding distortions of the ground truth segmentations. This step aids the neural network learning process, as it eliminates the need for rotational invariant features by ensuring that the LV will be in a similar location on each image, and the right and left ventricles will have the same orientation relative to each other. If tags such as "WindowCenter", "WindowLength", "RescaleSlope", and "RescaleIntercept" are included on the original file format (*e.g.*, DICOM), they are used to convert between raw signal intensities and display values, enhancing contrast and brightness.

As ground truth segmentations for cine images are more readily available, we aim to leverage them in our approach via a style transfer of cine images that generates pseudo-scar. Enhanced myocardium is generated by first randomly sampling from the known area of myocardium in a cine image. The area becomes a scar mask that is blurred using a Gaussian filter to smooth out edges. The bright scar mask is overlaid onto the original cine, which contains dark myocardium just as in LGE-CMR. Finally, we match intensity histograms to a random patient's LGE scan and add speckle noise.

## Model

### Stage 1: Left Ventricle Network

The objective of the left ventricle (LV) network (fig. 1A) is to reduce the background and clip the image to a square around the LV, allowing the second network to focus on identifying mostly myocardium-derived features. LV network inputs are enhanced to increase contrast between myocardium and blood pool by applying contrast-limited adaptive histogram equalization (CLAHE)<sup>35</sup>. Then, they are cropped or padded to a square of size  $192 \times 192$  pixels to eliminate potential aspect ratio distortion. Finally, each image slice scales between 0 and 255 based on the maximum and minimum intensity values of its cropped pixel array, excluding the added black space.

The LV network is a U-Net with residuals (ResU-Net) of depth four<sup>21,36</sup>. During the downsampling process, each of the four depth levels consists of 2 repetitions of a block of a  $3 \times 3$ , 2-D convolution, followed by a ReLU activation and batch normalization. After the second set of these three layers, each block ends with a  $2 \times 2$  max pooling layer and 20% dropout. A transition layer bridges the downsampling and upsampling branches, each of which contain similar blocks. However, upsampling is performed with a  $2 \times 2$  convolution (see supplementary fig. 5). Predictions are automatically cleaned up to identify the single component most likely to represent both the LV myocardium and bloodpool by performing slice- and volume-level checks (see code for further details upon publication).

### Stage 2: Myocardium Network

By cropping inputs to the second network around the LV identified in the first network, we substantially decrease class imbalance between myocardium and peripheral features of the scan. The cropped area is centered on a  $128 \times 128$  pixel image, and then intensities are scaled based on the histogram of the scan's entire volume rather than individually, as in the LV network. Volumetric scaling ensures consistency in the intensity contrast of scar and viable tissues. Notably, we do not perform CLAHE. Instead, we normalize the image intensities using the median intensity of the blood pool across the entire volume. Specifically, the following functions are applied sequentially to each input image component-wise:

$$\begin{aligned} I &\mapsto \frac{I}{2m_{I_{\mathcal{D}}}} \\ I &\mapsto 255 \times \frac{I - \min_{\mathcal{D}} I}{\max_{\mathcal{D}} I - \min_{\mathcal{D}} I} \\ I &\mapsto \min\{255, \max\{0, I\}\} \end{aligned}$$

where  $I$  is the image intensity,  $\mathcal{D}$  is the effective region following cropping by the LV network, and  $m_{I_{\mathcal{D}}}$  is the median signal intensity over  $\mathcal{D}$ .

Similarly to the LV network, we implement a ResU-Net structure with some modifications to identify the myocardium (fig. 1B). The myocardium network differs from the LV network in that it uses twice the number of filters at each of the 4 depth levels due to smaller image inputs (see fig. 5). It outputs two masks, one representing the entire myocardium and the other identifying only the non-viable tissue.

### Stage 3: Anatomical Autoencoder Post-Processing

This final neural network serves to adjust myocardial predictions such that they abide by anatomical guidelines. Expanding on the work in Painchaud *et al.*<sup>32</sup>, we develop a binary function  $\delta(\cdot)$  which uses different morphological operations to determine if a myocardium mask is anatomically correct. This function checks for convexity defects, holes in myocardium, circularity thresholds, number of objects, and myocardium thickness. The convolutional autoencoder is trained to reproduce myocardial segmentations after encoding them to a  $d$ -dimensional vector via a map  $\phi$  (fig. 6). Given the limited data, the low-dimensional vectors of the masks populating the latent space of the autoencoder may not be sufficient to capture the diverse geometries of valid segmentations. Therefore, the latent space is augmented with a large number of  $d$ -dimensional vectors,  $\mathbf{z}$ , such that when decoded by the network,  $\delta(\phi^{-1}(\mathbf{z})) = 1$ .

We fit a Gaussian mixture model (GMM) with  $k$  components to the training  $d$ -dimensional vectors in the latent space. We estimate  $k = 5$  and  $d = 16$  using the negative log likelihood (NLL) and adjusted Akaike information criterion (AIC)<sup>37</sup> by cross-validation on the training set. In order to avoid penalizing high dimensional fits with many small singular values in the covariance matrix, we adjust the AIC by scaling the number of parameters by the effective rank  $\text{Tr}(\Sigma)/\sigma_{\max}(\Sigma)$ , where  $\text{Tr}$  is the trace,  $\sigma_{\max}$  is the spectral norm, and  $\Sigma$  is the covariance matrix of a GMM component (fig. 4). When sampling from the new distribution, we reject a vector if, once decoded, the resulting mask does not pass the anatomical check  $\delta$ . This re-sampling scheme allows us to populate the latent space and will aid at prediction time. Once trained, the autoencoder's latent space is populated with vectors which are ensured to decode to anatomically correct masks. When predicting, a new — potentially incorrect — mask,  $\hat{I}$ , such mask is first encoded (fig. 1C) in the latent space to a vector  $\hat{\mathbf{z}} = \phi(\hat{I}) \in \mathbb{R}^d$ . Let the decoding function be  $\phi^{-1}$ . If  $\delta(\phi^{-1}(\hat{\mathbf{z}})) \neq 1$ , that is,  $\hat{I}$  does not encode and decode to an anatomically correct image, a nearest-neighbor algorithm is used to find the closest match  $\hat{\mathbf{z}}_{NN}$  in the latent space  $\hat{\mathbf{z}}_{NN} := \arg \min_{\mathbf{z}, \delta(\phi^{-1}(\mathbf{z}))=1} \|\mathbf{z} - \hat{\mathbf{z}}\|^2$ , where  $\mathbf{z}$  varies over the constructed couples that satisfy anatomical constraints. Lastly, we define the final, anatomically correct segmentation as  $\hat{I}' = \phi^{-1}(\hat{\mathbf{z}}^*)$ , where  $\hat{\mathbf{z}}^* = \hat{\mathbf{z}} + \alpha^*(\hat{\mathbf{z}} - \hat{\mathbf{z}}_{NN})$ , and  $\alpha^* = \arg \min_{\alpha \in [0,1]} \alpha$ , s.t.  $\delta[\phi^{-1}(\hat{\mathbf{z}} + \alpha(\hat{\mathbf{z}} - \hat{\mathbf{z}}_{NN}))] = 1$  (fig. 1D).

We highlight a few key advantages of the proposed algorithm over previous work. ACSNet uses a convolutional autoencoder with six  $3 \times 3$  convolutional layers paired with leaky ReLU activation to encode to 16-D vectors: this architecture has significantly lower capacity when contrasted with the ten-layer variational autoencoder implemented by Painchaud *et al.*<sup>32</sup> that derives a  $\sigma$  and  $\mu$  value for their 32-D latent distribution. Thus, ACSNet halves the number of latent dimensions used in Painchaud *et al.*<sup>32</sup>, demonstrating improved ability to represent images as smaller vectors. Further, one should be wary of the ability to generate more complex anatomical segmentations when re-sampling the space given the simple multi-variate normal assumption used in other work<sup>32</sup>. Our refined model of the distribution in encoded space allows for “C”-shaped myocardiums should these arise in basal slices.

Different experts may select different starting and stopping points when segmenting a patient's scan. To standardize our diverse data, we apply three additional volumetric checks that account for the excess of images often included in a CMR scan, those below the apex or above the base. We compare ratios of myocardial and blood pool area of each slice to identify the longest subsequence of relevant slices in the stack. Segmented volumes end at the index  $i = \max(i_M, \min(i_C + 1, i_D))$ . Here,  $i_M$  refers to the final index in the largest increasing subsequence by area;  $i_C$  represents the index of the first “C”-shaped slice (often associated with the basal region); and  $i_D$  represents the index of a large deviation of area between successive slices. This check allows incorporation of at most one “C”-shaped slice and prevents slices above the base with no true region of interest, often predicted incorrectly as a small or excessively large region. The decrease threshold for deviations, approximately 60%, represents the 95th percentile of the area difference between all sequential slices. Final volume object segmentations now pass per-slice and per-volume anatomical constraints.

### Training

In total, 2,484 2-D images were used for training and 269 LGE–CMR images were set aside for testing by randomly selecting 25% of the patients with LGE–CMR scans. Of note, there were no patients with multiple image modalities. No early stopping or other methods that learn from the validation set were used in training. All networks were trained on a NVIDIA Titan RTX GPU using Keras<sup>38</sup> and Tensorflow<sup>39</sup>. Training input to the LV network included 1,360 style-transferred ED cine-to-LGE images, as well as 1,124 LGE–CMR images, reserving 25% of the LGE–CMR scans for testing purposes. For the myocardium network, the training set used all patient scans with a corresponding scar segmentation, including style-transferred cine images with pseudo-scar. In total, all 1,355 style-transferred ED cine images and 744 of the LGE–CMR images were used in training with the same validation set withheld as for the LV network. Finally, the autoencoder used ED cine and all LGE–CMR ground truth myocardium masks in the training set.

Training of both the LV and the myocardium networks use the Adam optimizer<sup>40</sup>. To prevent cine-derived LGE images from dominating the training set, we weigh these accordingly in the loss function. Thus, the loss function used is a weighted combination of the balanced cross-entropy loss and the Tversky loss<sup>41</sup>:

$$l_1(p, \hat{p}) = -(\beta p \log(\hat{p}) + (1 - \beta)(1 - p) \log(1 - \hat{p}))$$

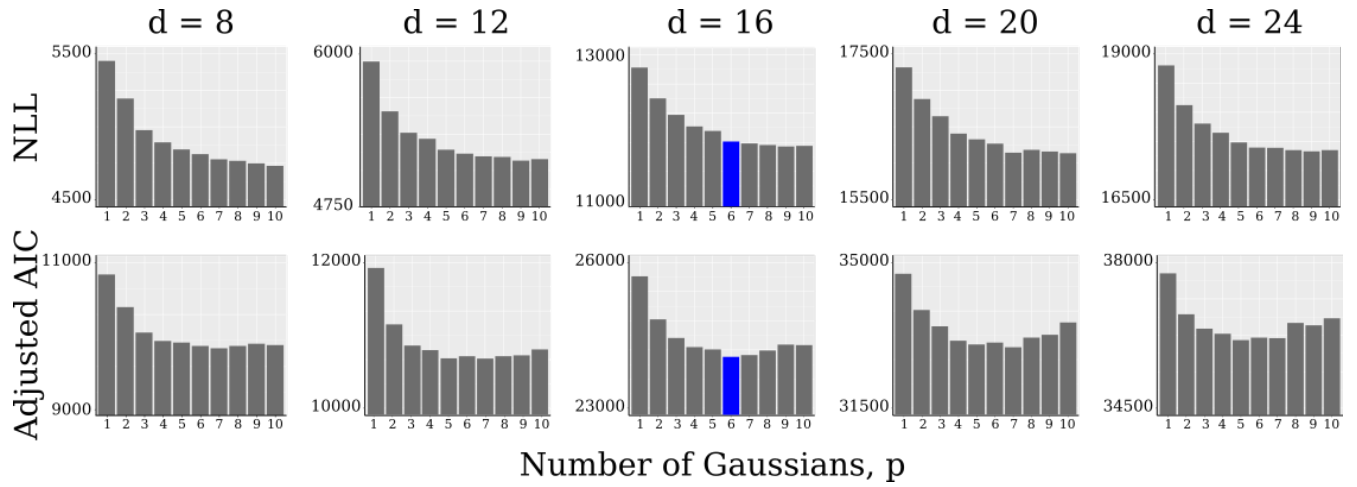


**Figure 4. Gaussian Mixture Model (GMM) for Latent Space.** A  $p$ -component (inset, x-axis) GMM is fit to the same training data used for the autoencoder. The negative log-likelihood (NLL, top row) and Akaike information criterion scaled by the effective rank (Adjusted AIC, bottom row) are calculated for various latent space dimensions  $d$  (columns) using 10-fold cross-validation. The dimension and number of components selected for the final model were  $d = 16$  and  $p = 6$  (blue) such that NLL plateaus, Adjusted AIC is minimized and  $d$  is high enough to ensure accurate reconstruction of the images by the autoencoder.

$$l_2(p, \hat{p}) = 1 - \frac{2TP(p, \hat{p})}{2TP(p, \hat{p}) + \beta FP(p, \hat{p}) + (1 - \beta)FN(p, \hat{p})},$$

where  $p$  and  $\hat{p}$  are pixel ground truth and predicted values, T/F P/N are true/false positive/negatives, and  $\beta$  is a weight on the false positives. We avoid over-cropping after the first network by using a  $\beta$  of 0.6 for LV identification and account for two outputs in the myocardium network, preferring fewer false positives, by using a  $\beta$  of 0.4. By optimizing over the mean of a per-pixel ( $l_1$ ) and per-image ( $l_2$ ) loss, each network is tailored towards the end goal of total myocardium segmentation.

## Evaluation

We evaluate standard imaging metrics to demonstrate the reliability of ACSNet across the entire heart. To do so, we calculate the Dice score of each slice prediction and use its location along the z-axis to place it into the first third, middle third, or upper third of the heart (corresponding to apex, middle, and base). The clinical applicability of ACSNet segmentations is demonstrated through consistently high performance as opposed to a high average with poor-performing outliers.

Additionally, we show low error in the calculation of LV volumes and quantification of scar using these segmentations. To calculate volume, nearest-neighbor interpolation is performed vertically across scans, while pixel spacing is accounted for in each slice. Volume includes myocardium and blood pool. When quantifying scar, it is noted that the ground truth fibrotic masks include both scar and gray zone. We assume, therefore, that the network picks up both areas of fibrotic tissue as well. Scar is often calculated using a threshold of the full width at half maximum (FWHM) of myocardium in LGE-CMR images<sup>42</sup>. By performing this threshold on both the scar predictions as well as the ground truth fibrotic segmentation, we successfully split the gray zone from the scar tissue. Finally, scar tissue quantification is calculated as the summation of the number of pixels above the FWHM threshold. Results for both LV volume and scar quantification are reported as relative MSE, which is the MSE divided by the  $\ell_2$  norm.

## References

1. Klem, I. *et al.* Assessment of myocardial scarring improves risk stratification in patients evaluated for cardiac defibrillator implantation. *J. Am. Coll. Cardiol.* **60**, 408–420, <https://doi.org/10.1016/j.jacc.2012.02.070> (2012).
2. Scott, P. A. *et al.* The extent of left ventricular scar quantified by late gadolinium enhancement mri is associated with spontaneous ventricular arrhythmias in patients with coronary artery disease and implantable cardioverter-defibrillators. *Circ. Arrhythmia Electrophysiol.* **4**, 324–330, <https://doi.org/10.1161/CIRCEP.110.959544> (2011).
3. Zipes, D. P. & Wellens, H. J. J. Sudden cardiac death. *Circulation* **98**, 2334–2351, <https://doi.org/10.1161/01.CIR.98.21.2334> (1998).



4. Roes, S. D. *et al.* Infarct tissue heterogeneity assessed with contrast-enhanced mri predicts spontaneous ventricular arrhythmia in patients with ischemic cardiomyopathy and implantable cardioverter-defibrillator. *Circ. Cardiovasc. Imaging* **2**, 183–190 (2009).
5. H.Kwon, D. *et al.* Extent of left ventricular scar predicts outcomes in ischemic cardiomyopathy patients with significantly reduced systolic function: A delayed hyperenhancement cardiac magnetic resonance study. *JACC Cardiovasc. Imaging* **2**, 34–44 (2009).
6. van der Burg, A. E. B. *et al.* Impact of viability, ischemia, scar tissue, and revascularization on outcome after aborted sudden death. *Circulation* **108**, 1954–1959, <https://doi.org/10.1161/01.CIR.0000091410.19963.9A> (2003).
7. Kim, R. J. *et al.* Relationship of mri delayed contrast enhancement to irreversible injury, infarct age, and contractile function. *Circulation* **100**, <https://doi.org/10.1161/01.CIR.100.19.1992> (1999).
8. Disertori, M. *et al.* Myocardial fibrosis assessment by lge is a powerful predictor of ventricular tachyarrhythmias in ischemic and nonischemic lv dysfunction: a meta-analysis. *JACC: Cardiovasc. Imaging* **9**, 1046–1055 (2016).
9. Mordi, I. *et al.* Lge and nt-probnp identify low risk of death or arrhythmic events in patients with primary prevention icds. *JACC: Cardiovasc. Imaging* **7**, 561–569 (2014).
10. Cain, M. A. *et al.* Cardiac sarcoidosis detected by late gadolinium enhancement and prevalence of atrial arrhythmias. *The Am. journal cardiology* **113**, 1556–1560 (2014).
11. Marra, M. P. *et al.* Impact of the presence and amount of myocardial fibrosis by cardiac magnetic resonance on arrhythmic outcome and sudden cardiac death in nonischemic dilated cardiomyopathy. *Hear. Rhythm*. **11**, 856–863 (2014).
12. Zhuang, X. Multivariate mixture model for cardiac segmentation from multi-sequence mri. *Int. Conf. on Med. Image Comput. Comput. Interv.* 581–588 (2016).
13. Zhuang, X. Multivariate mixture model for myocardial segmentation combining multi-source images. *IEEE Transactions on Pattern Analysis Mach. Intell. (T PAMI)* **41**, 2933–2946 (2019).
14. Campello, V. *et al.* Combining multi-sequence and synthetic images for improved segmentation of late gadolinium enhancement cardiac mri. *Pop M. et al. (eds) Stat. Atlases Comput. Model. Hear. Multi-Sequence CMR Segmentation, CRT-EPiggy LV Full Quantification Challenges. STACOM 2019. Lect. Notes Comput. Sci. vol 12009.* [https://doi.org/10.1007/978-3-030-39074-7\\_31](https://doi.org/10.1007/978-3-030-39074-7_31) (2020).
15. Suri, J. Computer vision, pattern recognition and image processing in left ventricle segmentation: The last 50 years. *Pattern Analysis Appl.* **3**, 209–242 (2000).
16. Huang, S. *et al.* An image-based comprehensive approach for automatic segmentation of left ventricle from cardiac short axis cine mr images. *J. Digit. Imaging* **4**, 598–608 (2011).
17. Suh, D. Y., Eisner, R. L., Mersereau, R. M. & Pettigrew, R. I. Knowledge-based system for boundary detection of four-dimensional cardiac magnetic resonance image sequences. *IEEE Transactions on Med. Imaging* **12**, 65–72 (1993).
18. et. al., Z. X. A global benchmark of algorithms for segmenting late gadolinium-enhanced cardiac magnetic resonance imaging. *arXiv* (2020).
19. Chen, C. *et al.* Deep learning for cardiac image segmentation: A review. *Front. Cardiovasc. Medicine* <https://doi.org/10.3389/fcvm.2020.00025> (2020).
20. Bello, G. A. *et al.* Deep-learning cardiac motion analysis for human survival prediction. *Nat. Mach. Intell.* **1**, 95–104, <https://doi.org/10.1038/s42256-019-0019-2> (2019).
21. Zheng, Q., Delingette, H., Duchateau, N. & Ayache, N. 3d consistent and robust segmentation of cardiac images by deep learning with spatial propagation. *IEEE Trans Med Imaging* (2018).
22. Yue, Q., Luo, X., Ye, Q., Xu, L. & Zhuang, X. Cardiac segmentation from lge mri using deep neural network incorporating shape and spatial priors. In *Medical Image Computing and Computer Assisted Intervention – MICCAI 2019*, vol. 11765 LNCS, 559–567, [10.1007/978-3-030-32245-8\\_62](https://doi.org/10.1007/978-3-030-32245-8_62) (Springer, 2019).
23. Roth, H., Zhu, W., Yang, D., Xu, Z. & Xu, D. Cardiac segmentation of lge mri with noisy labels. In Pop, M. *et al.* (eds.) *Statistical Atlases and Computational Models of the Heart. Multi-Sequence CMR Segmentation, CRT-EPiggy and LV Full Quantification Challenges*, 228–236 (Springer International Publishing, Cham, 2020).
24. Chen, C. *et al.* Unsupervised multi-modal style transfer for cardiac mr segmentation. *arXiv* (2019).

25. Zabihollahy, F., Rajchl, M., White, J. A. & Ukwatta, E. Fully automated segmentation of left ventricular scar from 3d late gadolinium enhancement magnetic resonance imaging using a cascaded multi-planar u-net (cmput-net). *Med. Phys.* **47**, 1645–1655, [10.1002/mp.14022](https://doi.org/10.1002/mp.14022) (2020).
26. Moccia, S. *et al.* Development and testing of a deep learning-based strategy for scar segmentation on cmr-lge images. *Magn. Reson. Mater. Physics, Biol. Medicine* **32**, 187–195 (2019).
27. Khened, M., Kollerathu, V. A. & Krishnamurthi, G. Fully convolutional multi-scale residual densenets for cardiac segmentation and automated cardiac diagnosis using ensemble of classifiers. *Med. image analysis* **51**, 21–45 (2019).
28. Bernard, O., Lalande, A., Zotti, C., Cervenansky, F. & *et al.* Deep learning techniques for automatic mri cardiac multi-structures segmentation and diagnosis: Is the problem solved? *IEEE Transactions on Med. Imaging* **37**, 2514–2525, [doi:10.1109/TMI.2018.2837502](https://doi.org/10.1109/TMI.2018.2837502) (2018).
29. Radau, P. *et al.* Evaluation framework for algorithms segmenting short axis cardiac mri. *The MIDAS J. - Cardiac MR Left Ventricle Segmentation Chall.* (2009).
30. Cheng, A. *et al.* Prospective observational study of implantable cardioverter-defibrillators in primary prevention of sudden cardiac death: study design and cohort description. *J. Am. Hear. Assoc.* **2**, [10.1161/JAHA.112.000083](https://doi.org/10.1161/JAHA.112.000083) (2013).
31. Ballistipedia. Bivariate. Retrieved from <http://ballistipedia.com/index.php?title=File:Bivariate.png> (2020).
32. Painchaud, N. *et al.* Cardiac mri segmentation with strong anatomical guarantees. *Shen D. et al. (eds) Med. Image Comput. Comput. Assist. Interv. - MICCAI 2019. MICCAI 2019. Lect. Notes Comput. Sci. vol 11765.* [https://doi.org/10.1007/978-3-030-32245-8\\_70](https://doi.org/10.1007/978-3-030-32245-8_70) (2019).
33. Larrazabal, A. J., Martínez, C., Glocker, B. & Ferrante, E. Post-dae: Anatomically plausible segmentation via post-processing with denoising autoencoders. *IEEE Transactions on Med. Imaging* 1–1 (2020).
34. Zhu, J.-Y., Park, T., Isola, P. & Efros, A. A. Unpaired image-to-image translation using cycle-consistent adversarial networks. In *Computer Vision (ICCV), 2017 IEEE International Conference on* (2017).
35. Pizer, S. M. *et al.* Adaptive histogram equalization and its variations. *Comput. vision, graphics, image processing* **39**, 355–368, [10.1016/S0734-189X\(87\)80186-X](https://doi.org/10.1016/S0734-189X(87)80186-X) (1987).
36. Ronneberger, O., Fischer, P. & Brox, T. U-net: Convolutional networks for biomedical image segmentation. *Navab N., Hornegger J., Wells W., Frangi A. (eds) Med. Image Comput. Comput. Interv. - MICCAI 2015. MICCAI 2015. Lect. Notes Comput. Sci. vol 9351* [https://doi.org/10.1007/978-3-319-24574-4\\_28](https://doi.org/10.1007/978-3-319-24574-4_28) (2015).
37. Akaike, H. A new look at the statistical model identification. *IEEE Transactions on Autom. Control.* **19**, 716–723 (1974).
38. Chollet, F. *et al.* Keras (2015).
39. Abadi, M. *et al.* TensorFlow: Large-scale machine learning on heterogeneous systems (2015). Software available from [tensorflow.org](https://www.tensorflow.org).
40. Kingma, D. & Ba, J. Adam: A method for stochastic optimization. *Int. Conf. on Learn. Represent.* (2014).
41. Salehi, S. S. M., Erdogmus, D. & Gholipour, A. Tversky loss function for image segmentation using 3d fully convolutional deep networks. *arXiv* (2017).
42. Mesubi, O. *et al.* Differences in quantitative assessment of myocardial scar and gray zone by lge-cmr imaging using established gray zone protocols. *Int J Cardiovasc. Imaging* **31**, 359–368, <https://doi.org/10.1007/s10554-014-0555-0> (2015).
43. Zhuang, X. *et al.* Cardiac segmentation on late gadolinium enhancement mri: A benchmark study from multi-sequence cardiac mr segmentation challenge. *arXiv* (2020).

## Acknowledgements

MM is grateful for support from the Simons Foundation, from NSF 2031985, 1934979, 1837991, and AFOSR FA9550-20-1-0288.

## Author contributions statement

DMP, HGA, MM and NAT designed the analysis. DMP and HGA developed the code and conducted the analysis. KCW provided annotated data. All authors wrote the manuscript.

## Competing interests

The authors have no competing interests to disclose.

## Supplementary Figures & Tables

Method	Dice Score	Hausdorff Distance (mm)
ACSNet	$0.79 \pm 0.024$	$6.76 \pm 0.46$
Interobserver <sup>12,13</sup>	$0.76 \pm 0.08$	$12.50 \pm 5.38$
Zabihollahy <i>et al.</i> <sup>25</sup>	$0.85 \pm 0.03$	$19.21 \pm 4.74$
Yue <i>et al.</i> <sup>22</sup>	$0.76 \pm 0.23$	$11.04 \pm 5.82$
Roth <i>et al.</i> <sup>23</sup>	0.78	16.30
Mean Result of MS-CMRSeg MICCAI Challenge <sup>43</sup>	$0.77 \pm 0.104$	$18.06 \pm 12.18$
Chen, Ouyang <i>et al.</i> <sup>24</sup>	$0.83 \pm 0.04$	$12.45 \pm 3.14$

**Table 1.** Comparison of LGE-CMR segmentation results for the LV myocardium. All entries were rounded from the provided values to the nearest tenths place. Note: These sources use different datasets; Data for Interobserver<sup>12,13</sup>, Yue *et al.*<sup>22</sup>, Roth *et al.*<sup>23</sup>, and Chen, Ouyang *et al.*<sup>24</sup> are based on the 2019 CMRSeg MICCAI challenge<sup>43</sup> consisting of 2-D LGE-CMR and corresponding steady-state free precision (bSSFP) from 45 patients, various subsets of whom were used to as test sets. Zabihollahy *et al.*<sup>25</sup> used three orthogonal views of 34 subjects with 3-D LGE-CMR scans.

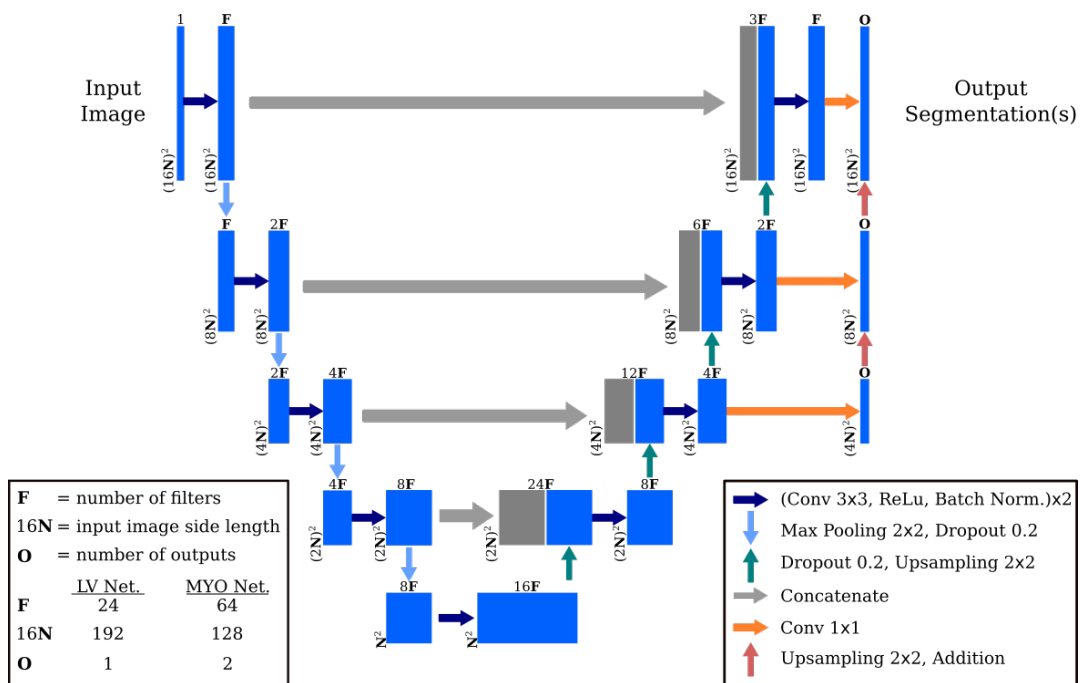


**Figure 5. Left Ventricle and Myocardium Network Architecture.** The left ventricle (LV) network identifies the main region of interest. The second network segments the myocardium (MYO) by differentiating between viable and non-viable tissue represented by each of the two outputs. The networks differ by the number of filters, input image size, and number of outputs as indicated. Both networks are U-Nets with residuals.

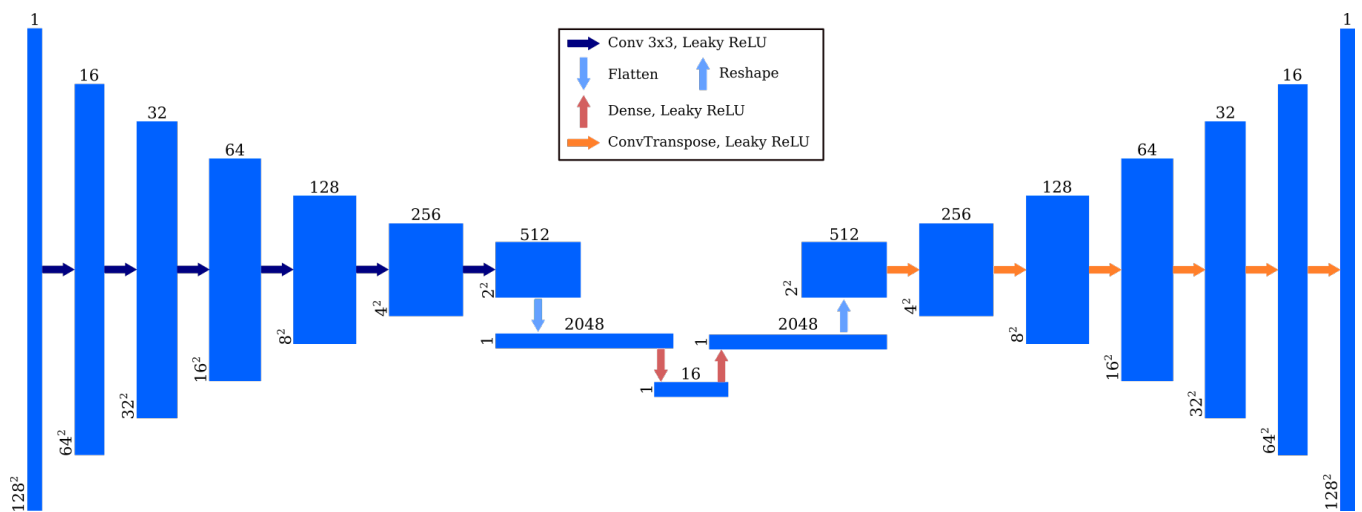


**Figure 6. Autoencoder Network Architecture.** The anatomical autoencoder serves as a post-processing step and can be thought of as a separate encoder and decoder.